Urban air mobility noise prediction in a 3D environment using Gaussian beam tracing

Yunusi Fuerkaiti[1], Damiano Casalino[1], Francesco Avallone[1] and Daniele Ragni[1]

[1]Aerodynamics, Wind Energy, Flight Performance and Propulsion Department, Delft
University of Technology, Delft 2629HS, the Netherlands
y.fuerkaitir@tudelft.com

Abstract

Numerical tools have been developed and applied for complex outdoor sound propagation problems based on the Gaussian Beam Tracing (GBT) method, a high-frequency approximate solution of the wave equation. However, due to various simplifications, particularly in the ray path tracing procedure, those tools show limitations for including atmospheric refraction effects due to 3D weather profiles in the noise propagation simulations. A new propagation model based on the GBT method that accounts for complex source directivity, the impact of 3D variation in the terrain geometry, and weather conditions in the simulation of noise propagation in an urban environment is presented in this work. The model takes a precomputed noise sphere as input and propagates it through a moving inhomogeneous atmosphere over realistic 3D terrain. The model is validated against the results of finite element solutions of a convected wave equation for various source frequencies, terrain geometries, and weather conditions; and is then applied to simulate the noise footprint of an electric vertical takeoff and landing aircraft hovering over a vertiport located in an urban setting. It is found that, compared to a quiescent atmosphere, the presence of the weather condition can contribute up to a 25 dB difference in the terrain and refractive shadow regions, suggesting the importance of including local weather conditions in the evaluation of urban air mobility noise. The results suggest that the present GBT acoustic propagation model can be applied to urban environments with advantages over conventional ray-tracing and full-wave solutions.

1 Introduction

Urban Air Mobility (UAM), powered with electric vertical takeoff and landing (eVTOL) vehicles, is anticipated to revolutionize transportation by extending it in three-dimension. Along with many expected benefits of UAM, such as faster commuting within a metropolitan area, UAM noise appears to be the main barrier to the community acceptance of UAM operations. Because these vehicles are expected to be first adopted for short-range low-altitude missions over densely populated areas not usually exposed to aircraft noise [1, 2]. As standards and regulations for UAM are yet to be developed and the community's opinion about these aircraft is still forming, it is crucial to address the noise impact of those aircraft as a priority. Therefore, in addition to the mitigation of noise at the source, it is necessary to accurately model noise propagation in urban environments considering various atmospheric and ground effects and evaluate the impact of noise on the community.

To accurately model noise propagation, it is necessary to include the most dominant factors: atmospheric (temperature and wind velocity gradients and fluctuations) and ground (topology, obstacles, vegetation, etc.) conditions. The former is responsible for the refraction of acoustic waves. In addition, random fluctuations of wind velocity and temperature due to atmospheric turbulent motion result in scattering of sound waves into refractive and terrain shadow regions (insonification) and coherence loss of the propagated noise signals. At the same time, the latter affects the reflection and diffraction of acoustic waves [3]. Considering scattering by atmospheric turbulence requires an additional level of sophistication of the prediction methods, which is beyond the scope of the present research.

Over the years, computational tools have been developed to simulate outdoor noise propagation. However, these tools show limitations in including atmospheric and ground effects when being adapted for predicting UAM noise propagation in complex outdoor environments. Noise-Power-Distance (NPD) data [4], which are specific to each aircraft, have been widely used to evaluate aircraft noise footprint. NPD estimates noise levels for a particular type of aircraft at a given flight condition, e.g., forward flight and distance from the observer. However, existing NPD data can not be employed to estimate the noise footprint of the UAM vehicles as they differ in many ways from conventional fixed-wing aircraft or rotary-wing aircraft, e.g., helicopters. In the absence of NPD, most approaches adopted to evaluate aircraft noise for different flight trajectories and operating conditions start from sampling noise sources over a sphere or hemisphere surrounding the aircraft. This approach has been widely used in the last years by several authors [5, 6, 7, 8]. The noise sources are then propagated on the ground either using the straight-ray propagation model with the assumption of constant weather conditions or using the curved-ray propagation model [7] that accounts for the sound wave refraction due to the wind and temperature gradients. Fast Field Program (FFP) [9] can account only for stationary source, layered atmosphere, and a homogeneous ground surface. Methods based on Parabolic Equation (PE) [10] are not optimal when considering moving sources [11] and computationally demanding at high-frequency range. On the other hand, methods based on the solution of wave equations using discretized versions of partial differential equations, for instance finite element or finite difference methods, can include these variations, but they are computationally demanding. Only a few examples are available restricted to relatively low-frequency problems [12, 13]. Contrarily to the methods mentioned above, ray-tracing is a widely used approach for studying sound propagation in a complex environment. The ray-tracing process hypothesizes the existence of sound rays propagating perpendicular to the wavefronts that provide a spatial depiction of sound travel and energy flow [14]. Ray-tracing has been shown to provide comparable results to wave-based methods for high-frequency problems. However, it is prone to numerical artifacts such as perfect shadow zone, and caustics [3, 15]. Ray-tracing predicts zero level in the shadow zone with a sharp discontinuity at the shadow boundary (perfect shadow zone); it predicts an infinite amplitude at locations where the ray tube cross-section area vanishes (caustics). On the other hand, Gaussian Beam Tracing (GBT) overcomes these difficulties by smoothing the transition between shadow and illuminated zone with a Gaussian decay and finite-amplitude at caoustics associated with a minimum beamwidth.

In beam tracing, beams are constructed around the central rays radiating from a source. A fan of such beams represents a point source, and the acoustic field at the receiver location is computed by coherently summing all contributing beams. As pointed out by authors [16, 17, 18], beam tracing has two remarkable advantages over classical ray tracing. First, beams smooth out singularities at caustics and shadow boundaries, thus providing more accurate results; second, it is more efficient if receivers distributed over a vast area are considered instead of a single point because eigenrays connect the source and the receivers do not need to be identified.

Although GBT was originally developed in geometrical optics, it has been modified and improved significantly in the seismic ray theories [19, 20] which formed the backbone of the GBT methods actively used in ocean [16, 18] and atmospheric [17, 21, 22] sound propagation applications. Based on the theories developed in geometrical optics, seismology, and ocean acoustics, Gabillet et al.[17] developed a 2D version of the GBT method and applied it for sound propagation in the atmosphere for the first time. A monopole source was employed, GBT predictions were compared against FFP, and experimental measurements and favorable agreement were found. One remarkable achievement of this work was the inclusion of diffraction with the uniform geometrical theory of diffraction[23]; it was shown that GBT appeared to be well suited to model the diffraction by a barrier above ground in the presence of a moving medium. However, the work did not mention multiple reflections over irregular surfaces. Mo et al.[21] developed a computational tool based on with GBT method for which the ray-paths were provided by an analytical ray tracer [24]. The advantage of this method was its efficiency in ray-path computation; however, the technique was restricted with constant gradient sound speed profiles and could not handle generic weather profiles. Bian et al. [22] developed a sound propagation model based on GBT that accounts for multiple reflections over irregular surfaces in a 3D environment. A rectilinear ray-tracer based on Snell's law was developed to provide a ray path for the GBT in a non-turbulent inhomogeneous medium. However, any refraction effect due to the variation in wind velocity was not considered. Furthermore, they did not mention the range-dependence of weather data in the presence of irregular ground surfaces.

Recently, Fuerkaiti et al. [7] developed a two-point 3D eigenray tracer that accounts for sound wave refraction due to vertical variability of air temperature and wind velocity gradients. They reported that the weather has a significant impact on long-range propagation, but it plays a small role in short-range propagation distances over a flat terrain [7]. However, local urban geometries highly distort wind velocity and temperature profiles in a realistic urban environment. They become range-dependent; therefore, complex propagation scenarios due to the combined effect of refraction, diffraction, multiple reflections, and their dependence on the propagation range would occur during the sound propagation.

The present work has two original contributions. The first one is the inclusion of the effect of 3D varying weather conditions on noise propagation in an urban environment. The second one is the inclusion of complex source directivity. The GBT method does not include complex source directivity by nature; instead, it assumes an omnidirectional point source such that the amplitude of each beam is identical in all directions. However, it is essential to include the complex source directivity for aircraft community noise predictions. All the work mentioned above did not address this limitation. Recently, Bian et al. [25] proposed a GBT-based model that incorporates complex source directivity through introducing a radiation function in the Gaussian beam summation formulation. As an alternative, a simple and efficient numerical approach has been developed in this work to incorporate the complex source directivity without modifying the original beam summation formulation.

The remainder of this paper is structured as follows. In section II, the numerical approach is described. In section III, validation and verification results are presented. Section IV shows the application in the noise footprint simulation of an eVTOL hovering in an urban environment. Finally, the conclusion of the work is given in Section V.

2 Numerical approach

A standard hybrid approach is used to predict the noise footprint of an aircraft in a 3D environment. The aforementioned numerical strategies and the GBT method are implemented in an in-house code universal acoustic ray and Gaussian beam tracer (UYGUR). A schematic illustration of the computational procedures is shown in Fig.1. First, a precomputed noise hemisphere/sphere is provided with the 3D wind and temperature profiles of the environment and the terrain geometry as inputs. The source noise hemisphere can be obtained by means of CFD simulation, experimental measurements, or efficient low-fidelity methods [8]. The ray tracing is then performed to determine the central ray associated with each Gaussian beam, followed by the dynamic ray tracing that accounts for the geometrical spreading and wavefront variation of sound waves in the vicinity of the central ray. Finally, the acoustic field at receiver points is calculated by summing the contribution of each Gaussian beam.

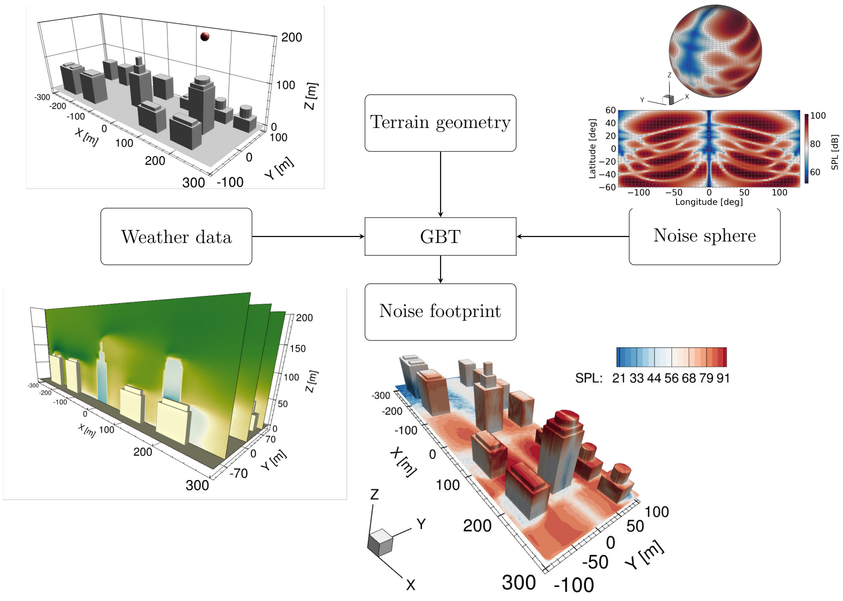

Figure 1: Schematic illustration of the computational procedures.

2.1 Reading 3D weather data

UYGUR reads 3D weather data as an ordered combination of 2D field slices sampled along the y-axis in a Cartesian coordinate system as shown in Fig. 1. The 2D field slices are sampled at a relatively shorter distance around the building corners, where substantial flow variation can be expected, and at a moderately larger distance if the space between two buildings is big and the variation in the flowfield is not significant. The temperature and wind velocity at any point between two adjacent slices is obtained through interpolation. For this purpose, barycentric polynomials [26] are employed. First, tabulated data points are used to evaluate relative distances between n points in a spatial dimension that forms a polynomial of order $n-1$. The interpolation and evaluation of temperature and wind velocity gradients are performed at a new point using the polynomial coefficients and polynomial derivatives.

As outlined by studies [26, 27], the barycentric interpolation method can be applied for a uniform or non-uniform grid of data points and is numerically stable, robust, and easy to implement for any number of dimensions.

2.2 Reading complex source directivity

The source noise is provided by a precomputed noise hemisphere containing the frequency and magnitude of noise radiated by the noise sources over a range of directions for a particular flight condition. In UYGUR, each Gaussian beam has the same initial amplitude and phase associated. To include complex source directivity, UYGUR reads source amplitudes and phase stored on the noise hemisphere at each ray-hemisphere intersection point and performs interpolation to estimate the amplitude and phase at the intersection point where noise signals are not available. Next, a correction is applied to include the loss within the source hemisphere radius such that the noise radiates from a point source. All processes are performed on the fly while rays are tracing, thus avoiding computational costs relevant to these processes.

2.3 Overview of the GBT approach

The first step of the GBT is to solve the the 3D acoustic ray-tracing system [28] to obtain the central ray of the beam. The 3D acoustic ray-tracing system reads:

$$\left.\begin{aligned} \frac{dx_i}{dt} &= \frac{c^2 k_i}{\Omega} + v_i \\ \frac{dk_i}{dt} &= -\frac{\Omega}{c}\frac{\partial c}{\partial x_i} - \sum_{j=1}^{3} k_j \frac{\partial v_j}{\partial x_i} \end{aligned}\right\} \tag{1}$$

Here, x_i is the ray path vector, and v_i is the medium velocity in the Cartesian coordinate system, t is time, c is the sound speed. The derivation of Eq.(7) and the relationships between wave-slowness vector k_i, and the parameter Ω are given in [28]. Eq.(7) is solved using a second-order Runge-Kutta scheme. A user-defined number of time steps is used to march the solution forward in time.

The Gaussian beam is then constructed around the central ray by solving the wave equation locally in ray-centered coordinates using the parabolic approximation. In a 3D medium, the ray-centered coordinates are represented by (q_1, q_2, s), where s is the arc-length along the central ray, and (q_1, q_2) are two normal distances from a field point to the central ray, which are defined as distances in the direction of the two mutually orthogonal unitary normal vectors $\boldsymbol{e}_1$ and $\boldsymbol{e}_2$ to the ray as shown in Fig. 2. In order to form the Gaussian beams in a 3D environment, it is essential to determine these unitary normal vectors, also known as polarization vectors. Cerveny et al. [29] derived a set of formulations that allows the evaluation of the polarization vectors at any point of a ray. Namely, the polarization vectors are related to the unitary tangent vector $\boldsymbol{t}$ along a ray path through the ray torsion and curvature, such that $\boldsymbol{e}_1$ and $\boldsymbol{e}_2$ are defined as follows:

$$\boldsymbol{e}_1 = \begin{bmatrix} e_{1x} \\ e_{1y} \\ e_{1z} \end{bmatrix} = \begin{bmatrix} (ck_1k_3\cos\phi + k_2\sin\phi)/L \\ (ck_2k_3\cos\phi - k_1\sin\phi)/L \\ cL\cos\phi \end{bmatrix}, \quad \boldsymbol{e}_2 = \begin{bmatrix} e_{2x} \\ e_{2y} \\ e_{2z} \end{bmatrix} = \begin{bmatrix} (ck_1k_3\sin\phi - k_2\cos\phi)/L \\ (ck_2k_3\sin\phi + k_1\cos\phi)/L \\ -cL\cos\phi \end{bmatrix} \tag{2}$$

where $L = \sqrt{(k_1^2 + k_2^2)}$ and ϕ is the rotation angle and given as:

$$\frac{d\phi}{ds} = \frac{k_3(k_2\partial c/\partial x - k_1\partial c/\partial y)}{L^2 c(s)} \tag{3}$$

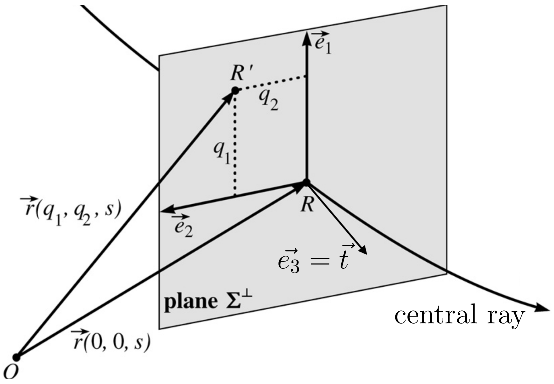

Figure 2: The ray-centered coordinates of a field point R' situated in the vicinity of a central ray (adapted from [19]). The field point R' is located on a plane perpendicular to the central ray crossing at point R.

With these equations, the polarization vectors can be easily determined at any point of a ray by integrating Eq. 3 together with the 3D ray-tracing system, thus avoiding computation of ray curvature and torsion [29].

In the second step, the dynamic ray tracing is performed to obtain the spreading and phase-front change of a Gaussian beam along the central ray. The dynamic ray-tracing system given by [30]

$$\left.\begin{aligned} \frac{dp_i}{ds} &= \frac{1}{c^2} c_{i,j} q_i, \quad i, j = 1, 2 \\ \frac{dq_i}{ds} &= c p_i \end{aligned}\right\} \tag{4}$$

where p_i describes beam slowness in a plane perpendicular to the propagation path, while q_i describes the beam spreading in the vicinity of the central ray along the propagation path, $c_{i,j}$ is a matrix of second derivatives of sound speed with respect to the two normal distances q_1 and q_2.

$$c_{i,j} = \begin{bmatrix} \dfrac{\partial^2 c(s)}{\partial q_1^2} & \dfrac{\partial^2 c(s)}{\partial q_1 \partial q_2} \\ \dfrac{\partial^2 c(s)}{\partial q_2 \partial q_1} & \dfrac{\partial^2 c(s)}{\partial q_2^2} \end{bmatrix} \tag{5}$$

Two linearly independent solutions are considered to obtain the Gaussian beam in a 3D environment [20]

$$\begin{bmatrix} \boldsymbol{P} \\ \boldsymbol{Q} \end{bmatrix} = \begin{bmatrix} p_1^{(1)} & p_1^{(2)} \\ p_2^{(1)} & p_2^{(2)} \\ q_1^{(1)} & q_1^{(2)} \\ q_2^{(1)} & q_2^{(2)} \end{bmatrix} \tag{6}$$

with the initial conditions

$$\begin{bmatrix} p_1^{(1)}(0) & p_1^{(1)}(0) \\ p_2^{(1)}(0) & p_2^{(1)}(0) \\ q_1^{(1)}(0) & q_1^{(1)}(0) \\ q_2^{(1)}(0) & q_2^{(1)}(0) \end{bmatrix} = \begin{bmatrix} 1 & 0 \\ 0 & 1 \\ \epsilon_1 & 0 \\ 0 & \epsilon_2 \end{bmatrix} \tag{7}$$

where $\epsilon_{1,2}$ are complex numbers that control the initial beamwidths in the two normal directions to the ray. The real and imaginary parts of $\epsilon_{1,2}$ allow independent control of both the beam width and the beam curvature, i.e., wavefront curvature. Once these equations are integrated along the central ray, the Gaussian beam can be formed as [18]

$$u_{beam}(q_1, q_2, s) = \frac{A(s)}{\sqrt{|\boldsymbol{Q}|}} e^{i\omega[\tau(s) + 0.5\boldsymbol{q}^T \boldsymbol{\Gamma}(s) \boldsymbol{q}]} \tag{8}$$

where $A(s)$ is the beam amplitude at s, $\tau(s)$ is the travel-time along the central ray, $\mathbf{\Gamma}(s) = \boldsymbol{P}(s)\boldsymbol{Q}^{-1}(s)$ is the 2×2 matrix of the second derivatives of the travel-time field with respect to the ray-centered coordinates and $\boldsymbol{q} = (q_1, q_2)^T$ is the distance vector. For a complete derivation of dynamic ray tracing, readers can refer to the book of Cerveny [19] and Popov [20].
When beams interact with environmental boundaries like irregular ground surfaces, terrain boundaries, etc., there is a jump in the sound speed gradient due to the discontinuity in the medium density such that the quantities $p_{i,j}$ and $q_{i,j}$ $(i, j = 1, 2)$ change discontinuously across those boundaries of the first or even second-order [30]. Hence, at points of incidence of a ray at an interface, the values of $p_{i,j}$ and $q_{i,j}$ must be updated. These new values will serve as the initial values for the solution of the dynamic ray tracing equations along with rays of reflected or transmitted waves. In this work, the formulae derived by Popov et al. [30] were used to update $p_{i,j}$ and $q_{i,j}$ at the points of incidence.

The final step of GBT is a superposition of all contributing Gaussian beams in the neighborhood of the receiver R'. The total field at a point located at the receiver R' reads

$$U(R', \omega) = \int\int \Phi(\alpha, \beta, \omega) u_{beam}(q_1, q_2, s) d\alpha d\beta \tag{9}$$

where α and β are the shooting angles in the elevation and azimuthal direction, respectively, of a ray with respect to an arbitrary axis passing through the source. The solution for a single beam is obtained by solving Eq.8 where $\Phi(\alpha, \beta, \omega)$ is called the weighting function. The weighting function is calculated by expanding the wavefield at the source and matching the high-frequency asymptotic behavior of the integral in Eq.9 to the exact solution for a source in a homogeneous medium [19].

3 Validation and Verification

In this section, UYGUR's capability to include complex source directivity is verified by comparing the acoustic footprint of a twin-propeller against reference data that was generated by $Opty\partial B$-FOOTPRINT tool [8]. Afterward, multiple reflections in an urban setting are validated by comparing GBT based predictions against full-wave solutions. For this purpose, the $Opty\partial B$-GFD tool that solves the Helmholtz equation using the Finite Element Method (FEM) is used to generate reference data. Lastly, range-dependent refraction due to 3D varying wind flow is validated by comparing the result against the reference predictions with a mean flow.

3.1 Reading complex source directivity

The source noise hemisphere is computed with the efficient low-fidelity approach [8] for a twin-propeller configuration operating at 2km, with an advance ratio $J = 0.84$. The distance between propellers is $2D$ (D propeller diameter), and the phase angle is $0°$. The noise hemisphere radius is $10D$. It is assumed that both propellers operate at the same RPM. The reference hemisphere for the first harmonics of BPF is shown in Fig.3a. The interference pattern due to the acoustic interaction of these two propellers is cleverly visible on the source hemisphere. The reference noise footprint is computed for receivers distributed over a square area 2.5 km by 2.5 km using the $Opty\partial B$-FOOTPRINT tool that propagates the sound rays towards the ground using straight rays [5, 7]. The noise footprints predicted with UYGUR and $Opty\partial B$-FOOTPRINT are compared and displayed in Fig.3b and Fig 3c, respectively. A favorable agreement is observed between the two that verifies the reliability of UYGUR for the inclusion of complex source directivity.

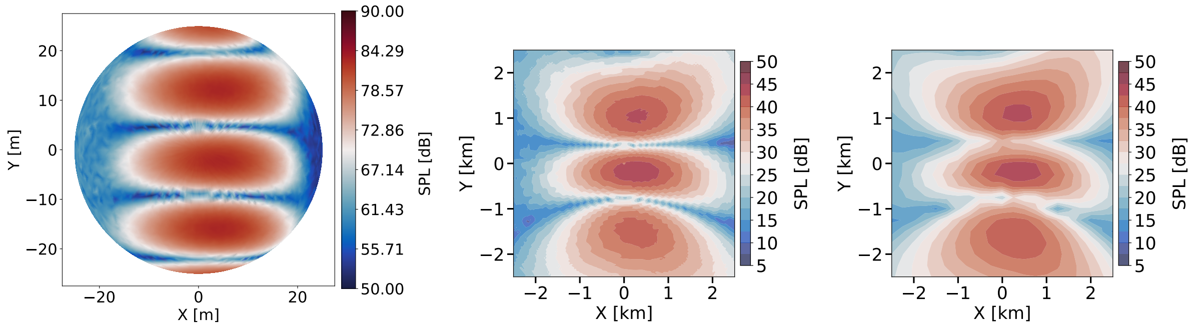

(a) (b) (c)

Figure 3: Bottom view of a reference noise hemisphere of a twin-propeller configuration (a). Noise footprint computed with UYGUR (b) and $Opty\partial B$-FOOTPRINT (c).

3.2 multiple reflection and range-dependent refraction

3.2.1 Case setup

As the present study focuses on predicting acoustic wavefields due to an elevated source, a time-harmonic monopole source located at (50,0,18) m and pulsating at 200 Hz is considered. Three-building blocks represent the urban area. The urban boundary is considered to be a perfect reflector; hence no acoustic energy is absorbed by the boundaries. The dimensions of the computational domain and the building blocks are listed in Table. 1. The acoustic wavefield is studied on two different receiver planes: xz-plane at y = 0 m and xy-plane at z = 10 m. The source-receiver geometry for the three-building configuration is displayed in Fig. 4.

Table 1: Dimensions of the computational domain and building blocks.

Domain	x [m]	length [m]	y [m]	width [m]	z [m]	height [m]
Computational domain	[0, 60]	60	[-10, 10]	20	[0, 20]	20
building 1	[8, 12]	4	[-4, 4]	8	[0, 12]	12
building 2	[28, 32]	4	[-4, 4]	8	[0, 12]	12
building 3	[36, 40]	4	[-4, 4]	8	[0, 12]	12

Two weather conditions, a moving atmosphere and a stationary atmosphere with a constant temperature of 15 °C are considered. The flowfield in the computational domain is resolved using the high-fidelity CFD solver SIMULIA PowerFLOW® based on the Lattice Boltzmann Very Large Eddy Simulation (LB/VLES) method, which is inherently unsteady and relies on an explicit time marching algorithm. One of the advantages of using PowerFLOW for urban wind simulations consists in the full automation of the volume mesh generation, which is created by the software around the imported geometries, by following user-defined regions of Variable Resolution (VR). A Cartesian mesh is employed by the Lattice-Boltzmann scheme with a resolution jump of factor 2 between adjacent VRs. In every VR, the time marching algorithm uses a local time step, thus resulting in a rate that is twice faster in a twice finer resolution region. The calculation load is automatically balanced among processors based on the so-called fine-equivalent number of voxels, i.e., the number of voxels multiplied by the ratio between the local resolution and the maximum resolution level. PowerFLOW is a leading market industrial CFD software, and its validation basis is very large, covering multiple application domains. Its description is outside the scope of the present work.

Three variable resolution layers (VRs) are used, with the smallest voxel size of 6.7 cm. This results in a total voxel count of 72 million within 70 million fine-equivalent voxels. The VRs are placed onto regions of interest, e.g., around the building edges as shown in Fig. 5a. The initial velocity is set to 5 m/s at the inlet, and the wind direction points to the positive x-axis direction. The mean flow required by the GBT and reference calculations is then acquired by time-averaging flow data sampled at multiple time frames. A snapshot of the mean flowfield on the vertical receiver plane for the three-building configuration is displayed in Fig. 5b.

The reference solution is obtained by using the frequency-domain FEM acoustic solver $Opty\partial B$-GFD and solving a second-order wave equation for the perturbation velocity potential in a non-uniform flow. An immersed boundary technique is used to avoid manual computational mesh generation for this specific study. The immersed boundary method relies on the intrinsic capabilities of a finite-element scheme of decoupling the nodes at which the solution is calculated from the points where an equation is satisfied. Therefore, the zero-normal derivative equation of the perturbation velocity potential (slip condition) is satisfied at the exact points of the imported immersed geometry, using the exact value of the surface normal. In order to improve the capability of the method to take into account the diffraction of an edge, when one mesh volume element is crossed by a wedge, one or more mutually unconnected virtual nodes are added to the volume mesh by duplication, and an equal number of new equations are added to the system. Every additional equation corresponds to the slip condition with a local value of the surface normal. The FEM code $Opty\partial B$-GFD has been validated for a variety of canonical problems [31, 32, 33] involving acoustic propagation in uniform and non-uniform flows, and its complete description is outside the scope of the present work.

In order to prevent any contamination due to possible reflected waves from the domain boundaries and ensure the PML layers absorb acoustic energy properly, the thickness of PML is set to 2 m. Moreover, the domain is discretized considering 9 points per wavelength to capture the wave interference pattern correctly.

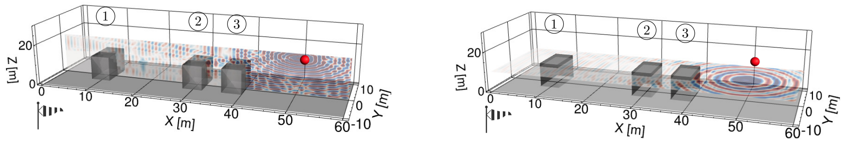

(a) XZ plane at y = 0 m. (b) XY plane at z = 10 m.

Figure 4: Source-receiver geometry. Vertical receiver plane (b) Horizontal receiver plane (b).

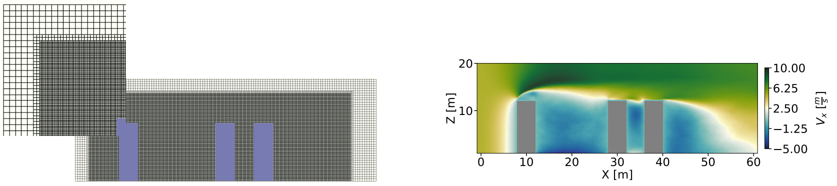

(a) VRs overview. (b) Wind velocity.

Figure 5: VRs overview (a). Snapshot of the mean flow field on the vertical receiver plane (b). Wind direction points to the positive x-axis.

3.2.2 Multiple reflections in homogeneous and stationary atmosphere

The comparisons between the two approaches at different observation planes are displayed in Fig. 6. GBT can capture the general trend of the interference pattern except for those between two adjacent building blocks. This is due to the diffracted sound waves into the building canyons, which are present in the reference result and are not included in the GBT model. The discrepancies at the receivers closer to the source are attributed to distortion of the pressure field by the diffracted sound waves from the edges of the third building closer to the source location in the reference result. The line plots showed a favorable agreement between the two approaches in terms of the pressure magnitude. The disparity in the phase is again attributed to the diffraction effects, which are not included in the GBT predictions.

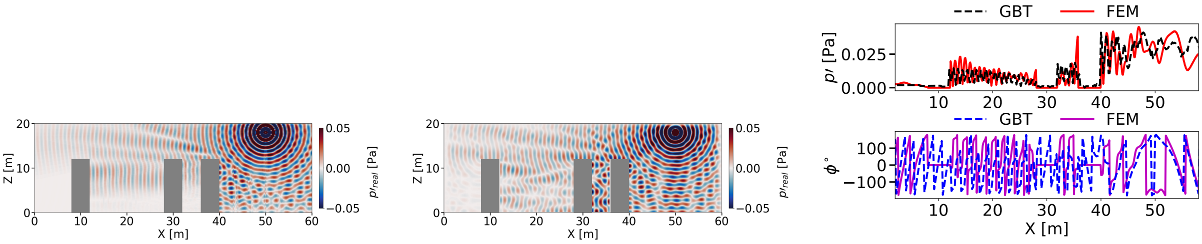

(a) GBT, f = 200 Hz.

(b) FEM, f = 200 Hz.

(c) z = 10 m, f = 200 Hz.

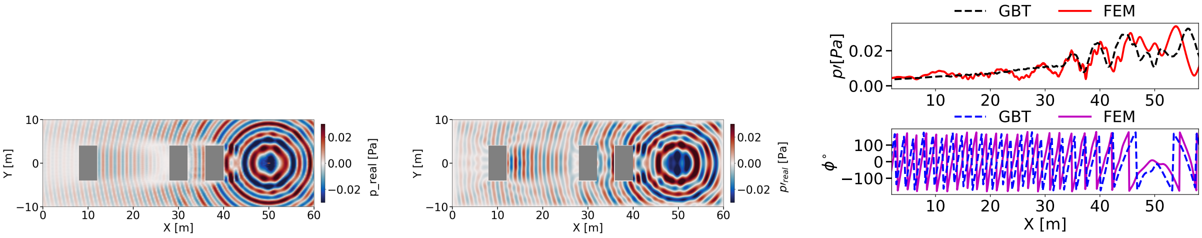

(d) GBT, f = 200 Hz.

(e) FEM, f = 200 Hz.

(f) y = 7 m, f = 200 Hz.

Figure 6: Comparison of UYGUR (GBT) and $Opty\partial B$-GFD (FEM) on the vertical and horizontal observation planes.

3.2.3 Multiple reflection and refraction due to inhomogeneous and moving atmosphere

The real values of the pressure field computed with the two approaches are compared on the vertical and horizontal receiver planes and displayed in Fig. 7. Compared to the same configuration but without mean flow, a noticeable observation is that the agreement between the two methods improved, as indicated by the line plots. This is because of the dependence of diffraction on the acoustic wavelength. When sound propagates against the wind, the wavefront has a local speed equal to $dx_i/dt = v_i + cn_i$ (see Eq.7), where $n_i = ck_i/\Omega$ is normal to the wavefront, that decreases along a ray path. The reduction in the local sound speed decreases the wavelength such that the diffraction becomes less visible. Furthermore, more substantial fluctuation in the pressure field between the second and third building blocks is seen. This is due to the variation in the local sound speed caused by the range-dependent wind flow, which eventually alters the acoustic wavelength; consequently, the acoustic wavelength approaches one of the harmonics of the resonance frequency, which leads to the formation of standing waves with large amplitude oscillations.

Moreover, it is noted that GBT predictions of complex pressure magnitude decay faster at receivers located farther away from the source in the upstream direction and raise considerably downstream direction. The decay and increase in acoustic pressure magnitude at upstream and downstream receivers, respectively, are expected. But this is more evident in GBT results than FEM predictions. This is likely due to various approximations implemented in GBT for reading and evaluating the temperature and wind velocity distribution in the 3D environment.

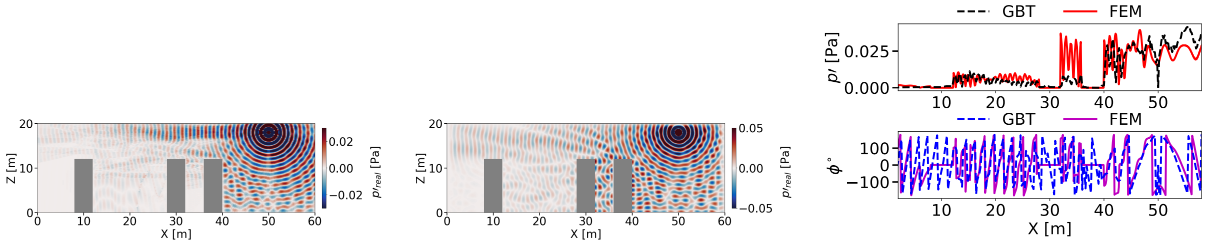

(a) GBT, f = 200 Hz.

(b) FEM, f = 200 Hz.

(c) z =10 m, f = 200 Hz.

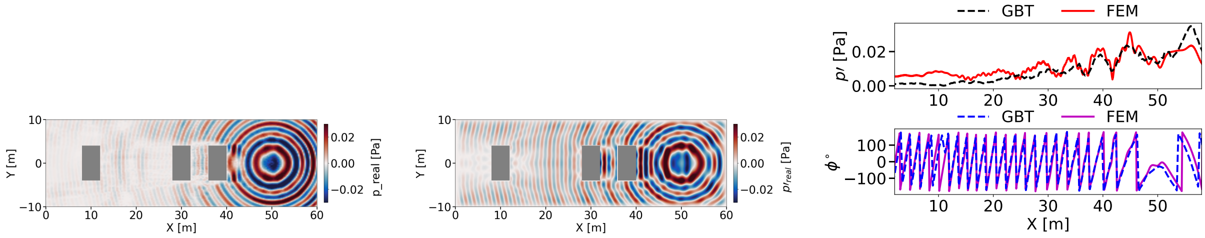

(d) GBT, f = 200 Hz.

(e) FEM, f = 200 Hz.

(f) y = 7 m, f = 200 Hz.

Figure 7: Comparison of UYGUR (GBT) and $Opty\partial B$-GFD (FEM) on the vertical and horizontal receiver plane in the presence of moving medium.

In general, a good agreement is found between the two approaches. It should be noted GBT is a high-frequency approximate solution of the wave equation that can give accurate results compared with the wave-based methods for higher frequency problems. However, the sound waves can be diffracted into the shadow regions behind the building blocks for lower frequencies, altering the field's interference pattern. Furthermore, refraction may either enhance or lessen the effect of diffraction as the wavelength of the local sound wave varies during propagation. Consequently, one may expect a slight deviation in the GBT prediction concerning the reference result. In the following, UYGUR is applied to predict the noise footprint of an eVTOL vehicle hovering over an urban environment.

4 Application

In this section, UYGUR's capability of including complex source directivity, multiple reflections due to irregular terrain surfaces, and refraction due to 3D variation in the wind flow is demonstrated by computing the noise footprint of an eVTOL vehicle hovering over a vertiport in an urban setting. The influence of local weather conditions on the noise footprint is highlighted by comparing the noise footprint calculated with and without weather conditions that can help engineers determine optimal locations for vertiports.

4.1 Case setup

As highlighted by the authors[34, 2], the spatial location of vertiports is vital for safer, faster, and more economical commuting within a city. Based on a survey reported in [2], 28% of people prefer to have vertiports over building rooftops that could reduce nuisance due to the vertiport's high traffic density. 65 % of people like to have vertiports closer to transportation hubs in a city center due to economic reasons and efficiency in total travel time. Based on these preferences, this study considers a vertiport located on the rooftop of a high-rise building in an urban setting representative of a typical city center with many transportation hubs as shown in 8a. The wind field in the metropolitan area is resolved using the high-fidelity CFD solver SIMULIA PowerFLOW® for an initial wind velocity of 5 m/s that points to the positive x-axis direction. Snapshots of the wind field on xy-plane at z = 55 m and on xz-plane at y = 0 m are displayed in Fig. 8b and Fig. 8c, respectively, that show how the local building geometries distort the wind field.

A quadrotor-like eVTOL vehicle, similar to the one presented in [35], is considered. The vehicle's gross weight is assumed to be 629 kg that can carry a max of two people. The eVTOL is powered with four rotors, as shown in Fig. 9a. Each rotor has three blades, and the blade has the same radial distribution of twist angle and chord length as the one described in [36]. The rotor diameter D is 1.8 m. In the local reference system of the vehicle, the relative distance between the two rotors along the y-axis is set to $2D$ to avoid aerodynamic interference. At the same time, the distance between the rotors along the x-axis is set to $3D$. The rear rotors, i.e., rotors at the negative x-axis part of the reference system, are elevated by $0.8D$ with respect to the front rotors to decrease the aerodynamic interaction between front, and rear rotors [35]. The source sphere radius is set to $23D$. 74 meridians, and 74 parallels are used to discretize the sphere to capture the complex source directivity on the sphere accurately. The vehicle is hovering at the position (200, 0, 200) m over the vertiport, as shown in Fig.8a. It is assumed that all four rotors rotate at the same rotational speed. Moreover, the total required thrust is distributed evenly at all rotors. Each rotor generates 1/4 of the target thrust, i.e., 1540 N, which is achieved by trimming the rotor blade pitch angle for a given rotor speed of 3000 RPM. Finally, the source noise sphere is computed using the low-fidelity toolchain outlined in [8] that accounts for steady loading noise, thickness noise, and turbulent boundary layer trailing edge noise. Here, the source noise spheres corresponding to the first and second harmonics of Blade Passing Frequency (BPF) 150 Hz are considered; the resulting acoustic spheres are plotted using the equidistant cylindrical projection [37] and displayed in Fig. 9b and Fig. 9c, respectively. As the eVTOL fuselage does not significantly impact acoustics [35], and the rotors are the primary noise source, noise scattered by the airframes is neglected.

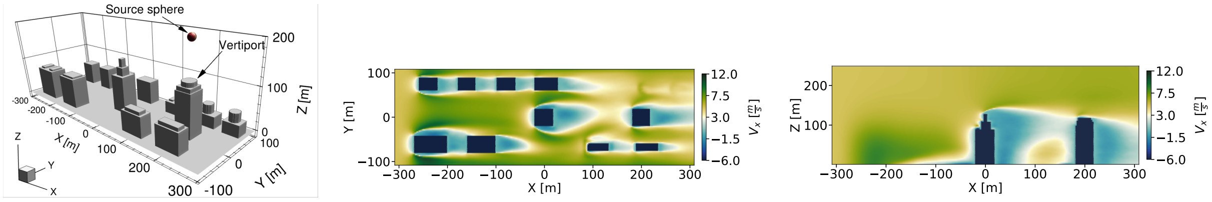

(a)

(b)

(c)

Figure 8: Geometry of the problem (a). Snapshots of mean flow on the xy-plane at z = 55 m (b) and on the xz-plane at y = 0 m (c). Wind direction points to the positive x-axis.

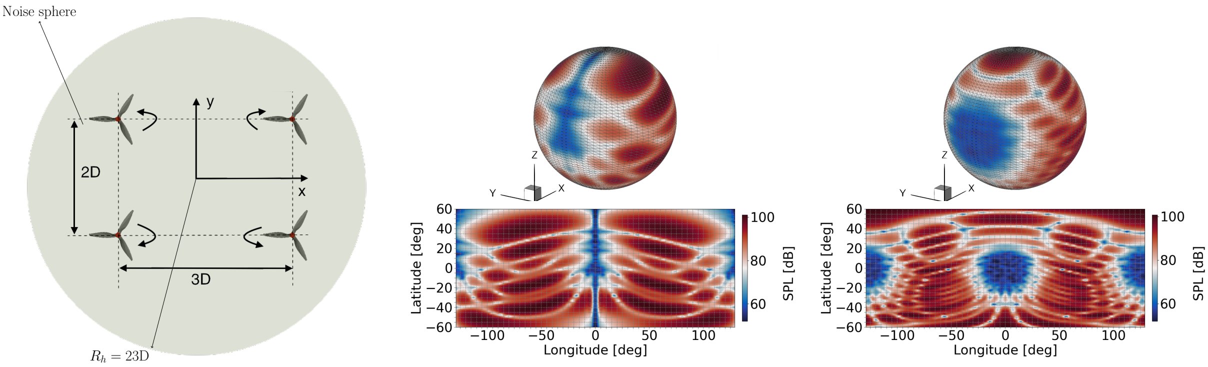

(a) Top view.

(b) 1 BPF.

(c) 2 BPF.

Figure 9: The geometry of the source noise sphere, the eVTOL vehicle's four propellers, and the reference system (a). SPL computed over the noise sphere for 1 BPF (b) and 2 BPF (c).

4.2 Results

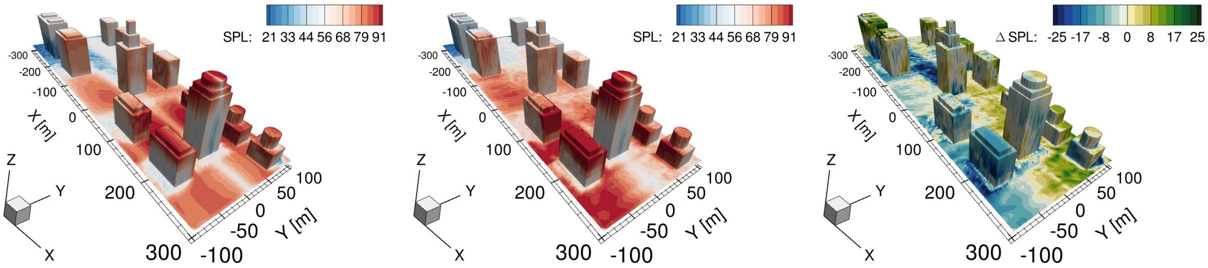

(a) (b) (c) $\Delta = (a) - (b)$

Figure 10: Noise footprint of the eVTOL in a quiescent atmosphere (a) and in a moving inhomogeneous atmosphere (b) and the field difference between them (c) for 1 BPF.

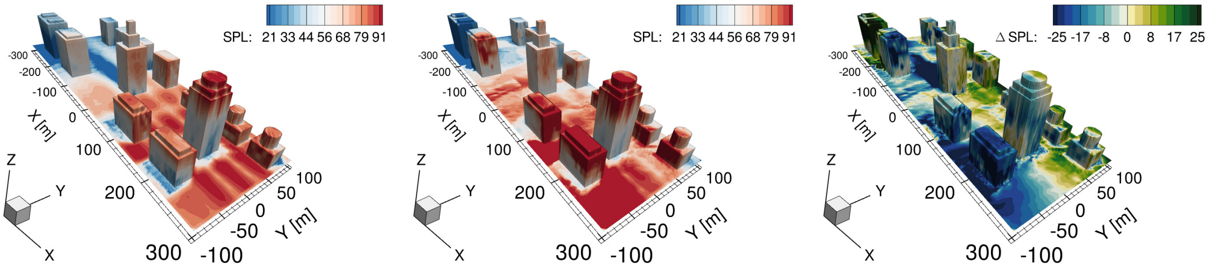

(a) (b) (c) $\Delta = (a) - (b)$

Figure 11: Noise footprint of the eVTOL in a quiescent atmosphere (a) and in a moving inhomogeneous atmosphere (b) and the field difference between them (c) for 2 BPF.

The noise footprints of the eVTOL in a quiescent atmosphere and in the presence of wind and the field difference between these two are computed for the first and second harmonics of BPF and displayed in Fig. 10 and Fig 11, respectively. For 1 BPF, compared to the one in a quiescent atmosphere, the on-ground noise levels in the presence of wind increased considerably in the region enclosed by x = [-100, 300] m and y = [-100,-25], particularly behind the building at the center of the domain and the two buildings located at (100,-60,0) m and (200,-60,0) m, respectively. As shown in Fig. 10a, those regions are seen as shadow zones, and due to the presence of the weather condition, sound rays are refracted into those regions, eventually raising the noise levels. As highlighted in [7], the weather has a significant impact on the predicted noise footprint at longer distances. This is also observed in Fig. 10b, where the noise levels drop significantly at the rooftop of the farthest building located at (-250,-60,0) m. This is attributed to the refractive shadow zone that occurs when the source-receiver distance is a few times larger than the source height, and the local sound speed decreases towards the receiver. The difference in the noise footprints is obtained by subtracting the noise levels in a realistic weather condition from the quiescent one; thus, the negative values indicate higher noise levels in the presence of weather conditions. As seen, the presence of the wind can contribute up to 25 dB in the predicted noise footprint mainly distributed in the terrain shadow and refractive shadow regions, implying the ground noise levels are highly dependent on the local weather data. Similar trends are observed for 2 BPF; however, the field difference, particularly in those shadow regions, becomes even more prominent due to the variation in the source directivity.

A big difference in the predicted footprints with and without weather conditions can be expected, particularly at the terrain and refractive shadow regions. Nevertheless, in a more realistic scenario considering the effects of diffraction and atmospheric turbulence, the difference would be smaller than 25 dB.

5 Conclusion

A new propagation model based on GBT that includes sound wave refraction and multiple reflections due to the variation in the weather conditions and ground topology, respectively, is developed and presented in this work.

The propagation model is validated against the results of various ray-based and wave-based methods. The validation results demonstrated that the propagation model could accurately account for complex source directivity and be readily applied for high-frequency problems in aircraft community noise predictions. Furthermore, the noise footprint of the eVTOL in the presence of weather conditions reveals the significant importance of including local weather effects in the evaluation of eVTOL noise impact on the community.

The GBT approach in this work does not include diffraction effects. As the results demonstrated, more comprehensive models need to be developed to include the diffraction effects for lower frequency problems. Furthermore, the influence of atmospheric turbulence on propagation is ignored. More sophisticated models are needed to predict the wavefield in the shadow zones due to sound wave scattering by atmospheric turbulence.

References

[1] SA Rizzi, DL Huff, D Boyd, P Bent, B Henderson, KA Pascioni, C Sargent, DL Josephson, M Marsen, H He, et al. Urban air mobility noise: Current practice, gaps, and recommendations. Technical report, NASA TP-2020-5007433, 2020.

[2] Ender Çetin, Alicia Cano, Robin Deransy, Sergi Tres, and Cristina Barrado. Implementing mitigations for improving societal acceptance of urban air mobility. *Drones*, 6(2):28, 2022.

[3] Erik M Salomons. *Computational Atmospheric Acoustics*. Springer Science & Business Media, 2001.

[4] ECAC. ECAC.CEAC Doc. 29. report on standard method of computing noise contours around civil airports. volume 2: Technical guide. Technical report, European Civil Aviation Conference (ECAC), 2016.

[5] Damiano Casalino, Wouter C van der Velden, and Gianluca Romani. Community noise of urban air transportation vehicles. In *AIAA Scitech 2019 Forum*, page 1834, 2019.

[6] Zhongqi Jia and Seongkyu Lee. Acoustic analysis of urban air mobility quadrotor aircraft. In *Vertical Flight Society (VFS) Aeromechanics for Advanced Vertical Flight Technical Meeting*, 2020.

[7] Yunusi Fuerkaiti, Damiano Casalino, Francesco Avallone, and Daniele Ragni. Toward inclusion of atmospheric effects in the aircraft community noise predictions. *The Journal of the Acoustical Society of America*, 150(2):759–768, 2021.

[8] Y. Fuerkaiti, E. Grande, D Casalino, F. Avallone, and D. Ragni. Efficient low-fidelity aeroacoustic permanence calculation of propellers. *Aerospace Science and Technology: Under Review*, 2022.

[9] S. J. Franke and Swenson G. W. A brief tutorial on the fast field program (ffp) as applied to sound propagation in the air. *Applied Acoustics*, 27:203–215, 1989.

[10] Kenneth E Gilbert and Michael J White. Application of the parabolic equation to sound propagation in a refracting atmosphere. *The Journal of the Acoustical Society of America*, 85(2):630–637, 1989.

[11] Sebastian Ghinet, Andrew Price, Gilles A Daigle, Michael R Stinson, Anant Grewal, and Viresh Wickramasinghe. Atmospheric propagation of aircraft acoustic signature from high altitude. In *INTER-NOISE and NOISE-CON Congress and Conference Proceedings*, volume 259, pages 4654–4665. Institute of Noise Control Engineering, 2019.

[12] Damiano Casalino, Mattia Barbarino, and Antonio Visingardi. Simulation of helicopter community noise in complex urban geometry. *AIAA journal*, 49(8):1614–1624, 2011.

[13] Damiano Casalino, Wouter C van der Velden, Gianluca Romani, and Ignacio Gonzalez-Martino. Aeroacoustic analysis of urban air operations using the lb/vles method. In *25th AIAA/CEAS Aeroacoustics Conference*, page 2662, 2019.

[14] J. S. Lamancusa and P. A. Daroux. Ray tracing in a moving medium with two-dimensional sound speed variation and application to sound propagation over terrain discontinuities. *J Acoust Soc Am*, 93:1716–1726, 1993.

[15] Vladimir E Ostashev and D Keith Wilson. *Acoustics in moving inhomogeneous media*. CRC Press, 2nd edition, 2015.

[16] Michael B Porter and Homer P Bucker. Gaussian beam tracing for computing ocean acoustic fields. *The Journal of the Acoustical Society of America*, 82(4):1349–1359, 1987.

[17] Yannick Gabillet, Hartmut Schroeder, Gilles A Daigle, and André L'Espérance. Application of the gaussian beam approach to sound propagation in the atmosphere: Theory and experiments. *The Journal of the Acoustical Society of America*, 93(6):3105–3116, 1993.

[18] Michael B Porter. Beam tracing for two-and three-dimensional problems in ocean acoustics. *The Journal of the Acoustical Society of America*, 146(3):2016–2029, 2019.

[19] Vlastislav Cervenỳ. *Seismic ray theory*, volume 110. Cambridge university press Cambridge, 2001.

[20] Mikhail Mikhailovich Popov. *Ray theory and Gaussian beam method for geophysicists*. Edufba, 2002.

[21] Qi Mo, Hengchin Yeh, Ming Lin, and Dinesh Manocha. Outdoor sound propagation with analytic ray curve tracer and gaussian beam. *The Journal of the Acoustical Society of America*, 141(3):2289–2299, 2017.

[22] Haoyu Bian, Ryu Fattah, Siyang Zhong, and Xin Zhang. An efficient rectilinear gaussian beam tracing method for sound propagation modelling in a non-turbulent medium. *The Journal of the Acoustical Society of America*, 148(6):4037–4048, 2020.

[23] Robert G Kouyoumjian and Prabhakar H Pathak. A uniform geometrical theory of diffraction for an edge in a perfectly conducting surface. *Proceedings of the IEEE*, 62(11):1448–1461, 1974.

[24] Qi Mo, Hengchin Yeh, and Dinesh Manocha. Tracing analytic ray curves for light and sound propagation in non-linear media. *IEEE transactions on visualization and computer graphics*, 22(11):2493–2506, 2015.

[25] Haoyu Bian, Ryu Fattah, Siyang Zhong, and Xin Zhang. On the efficient modeling of generic source directivity in gaussian beam tracing. *The Journal of the Acoustical Society of America*, 149(4):2743–2751, 2021.

[26] Orlando Camargo Rodríguez, Jon M Collis, Harry J Simpson, Emanuel Ey, Joseph Schneiderwind, and Paulo Felisberto. Seismo-acoustic ray model benchmarking against experimental tank data. *The Journal of the Acoustical Society of America*, 132(2):709–717, 2012.

[27] Rogério de Moraes Calazan. Numerical enhancements and parallel gpu implementation of the traceo3d model. 2018.

[28] Allan D Pierce. *Acoustics: an introduction to its physical principles and applications*. Springer, 3rd edition, 2019.

[29] V Červenỳ and F Hron. The ray series method and dynamic ray tracing system for three-dimensional inhomogeneous media. *Bulletin of the Seismological Society of America*, 70(1):47–77, 1980.

[30] MM Popov, Ivan Pšenčík, and V Červenỳ. Computation of ray amplitudes in inhomogeneous media with curved interfaces. *Studia Geophysica et Geodaetica*, 22(3):248–258, 1978.

[31] Damiano Casalino. Reprint of: Benchmarking of different wave models for sound propagation in non-uniform flows. *Procedia IUTAM*, 1:163–172, 2010.

[32] Damiano Casalino. Finite element solutions of a wave equation for sound propagation in sheared flows. *AIAA journal*, 50(1):37–45, 2012.

[33] Damiano Casalino, Samuele Santini, Mariano Genito, and Valerio Ferrara. Rocket noise sources localization through a tailored beam-forming technique. *AIAA journal*, 50(10):2146–2158, 2012.

[34] Mihir Rimjha, Mia Li, Nick Hinze, Sayantan Tarafdar, Susan Hotle, H Swingle, A Trani, and Jeremy Christopher Smith. Demand forecast model development and scenarios generation for urban air mobility concepts. 2020.

[35] Zhongqi Jia and Seongkyu Lee. Acoustic analysis of a quadrotor evtol design via high-fidelity simulations. In *25th AIAA/CEAS Aeroacoustics Conference*, page 2631, 2019.

[36] D. Casalino, G. Edoardo, G. Romani, D. Ragni, and F. Avallone. Definition of a benchmark for low reynolds number propeller aeroacoustics. *Aeroaspace Science and Technology*, 2021.

[37] John Parr Snyder. *Map projections–A working manual*, volume 1395. US Government Printing Office, 1987.